

Structured polarized light microscopy for collagen fiber structure and orientation quantification in thick ocular tissues

Bin Yang
Bryn Brazile
Ning-Jiun Jan
Yi Hua
Junchao Wei
Ian A. Sigal

Structured polarized light microscopy for collagen fiber structure and orientation quantification in thick ocular tissues

Bin Yang,^a Bryn Brazile,^a Ning-Jiun Jan,^{a,b} Yi Hua,^a Junchao Wei,^a and Ian A. Sigal^{a,b,*}

^aUniversity of Pittsburgh School of Medicine, Department of Ophthalmology, Pittsburgh, Pennsylvania, United States

^bUniversity of Pittsburgh, Department of Bioengineering, Pittsburgh, Pennsylvania, United States

Abstract. Collagen is a major constituent of the eye and understanding its architecture and biomechanics is critical to preserve and restore vision. We, recently, demonstrated polarized light microscopy (PLM) as a powerful technique for measuring properties of the collagen fibers of the eye, such as spatial distribution and orientation. Our implementation of PLM, however, required sectioning the tissues for imaging using transmitted light. This is problematic because it limits analysis to thin sections. This is not only slow, but precludes study of dynamic events such as pressure-induced deformations, which are central to the role of collagen. We introduce structured polarized light microscopy (SPLM), an imaging technique that combines structured light illumination with PLM to allow imaging and measurement of collagen fiber properties in thick ocular tissues. Using pig and sheep eyes, we show that SPLM rejects diffuse background light effectively in thick tissues, significantly enhancing visualization of optic nerve head (ONH) structures, such as the lamina cribrosa, and improving the accuracy of the collagen fiber orientation measurements. Further, we demonstrate the integration of SPLM with an inflation device to enable direct visualization, deformation tracking, and quantification of collagen fibers in ONHs while under controlled pressure. © 2018 Society of Photo-Optical Instrumentation Engineers (SPIE) [DOI: [10.1117/1.JBO.23.10.106001](https://doi.org/10.1117/1.JBO.23.10.106001)]

Keywords: polarized light microscopy; structured light illumination; collagen fiber structure; collagen fiber orientation; biomechanics; eye; sclera.

Paper 180426R received Jul. 2, 2018; accepted for publication Sep. 13, 2018; published online Oct. 1, 2018.

1 Introduction

As a major constituent of the eye, collagen fibers are organized into highly complex structures with distinct mechanical and optical properties essential to the normal ocular functions.^{1,2} Recent studies suggest that collagen fibers play an important role in several ocular diseases, such as glaucoma,^{3,4} myopia,⁵ and keratoconus.^{6,7} Understanding its architecture and biomechanics is thus critical to preserve and restore vision.

Polarized light microscopy (PLM) has recently been demonstrated to be a powerful and robust technique for measuring properties of collagen fibers in ocular tissues, allowing the visualization and analysis of collagen fiber anisotropy,⁸ orientation,^{9,10} and of microstructural crimp in the posterior pole¹¹ and around the globe in sheep¹² and in humans.¹³ Our implementations of PLM, however, require sectioning the tissue for imaging using transmitted light, usually after fixation. This is slow, destructive, and limits the analysis to thin sections. More importantly, it precludes the study of dynamic events such as pressure-induced deformations, which are essential to understand eye biomechanics and the role of collagen.^{14–16} Extending PLM imaging from thin sections to thick ocular tissues is thus desirable. However, imaging thick tissues is complicated by strong tissue scattering.¹⁷ Specifically for PLM, multiple scattering introduces nonspecific changes to the polarization state of the reflected light, which causes artifacts in quantification and visualization of fiber properties. To overcome this challenge, we introduce structured polarized

light microscopy (SPLM) imaging, a reflected light imaging technique that combines structured light illumination¹⁸ with PLM. SPLM effectively rejects diffuse background light interfering with the polarization analysis and preserves light encoded with useful tissue birefringence information, thus enabling the visualization and quantification of collagen fibers of thick ocular tissues.

In this work, we demonstrate and validate the performance of SPLM as a robust imaging technique for assessing collagen fiber properties of thick ocular tissues. Furthermore, we demonstrate the integration of SPLM with an inflation device for direct visualization and deformation tracking of optic nerve head (ONH) structures, such as the lamina cribrosa. Finally, we discuss the strengths and limitations of SPLM relative to some of the most commonly used techniques to study ocular tissues.

2 Methods

2.1 Sample Preparation and Mounting

We used eyes from sheep and pig under 2-years-old obtained from a local slaughterhouse within 6-h of death. The posterior pole connective tissues of pig and sheep eyes have been shown to be similar to those of humans.^{19–21} To demonstrate that SPLM imaging is appropriate for different species and for both fresh and fixed tissue, the pig eyes were imaged in their fresh state, whereas the sheep eyes were fixed in 10% formalin for 24 h⁹ before imaging. We have shown that fixation only causes minimal changes in the overall shape or size of tissues,²² and in

*Address all correspondence to: Ian A. Sigal, E-mail: ian@ocularbiomechanics.com

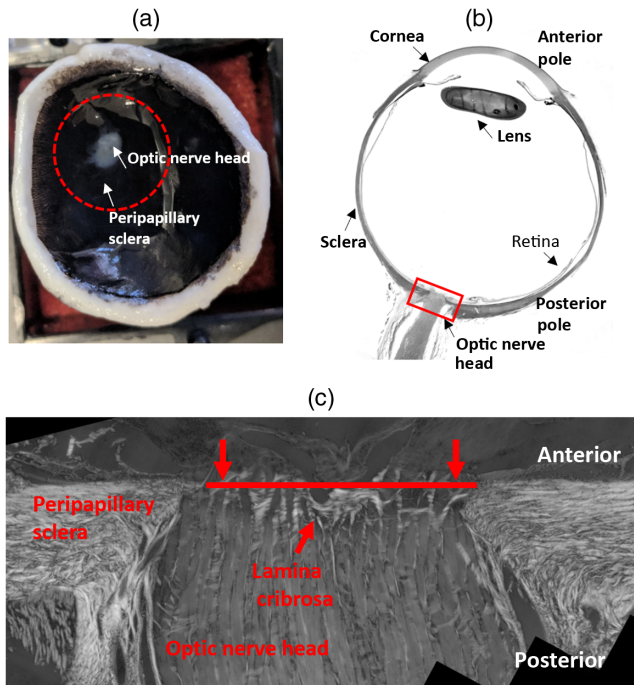


Fig. 1 (a) Top view of the posterior pole of the eye. The red dashed-circle indicates the trephined region. (b) Anatomy of the eye (sagittal view). The red box indicates the ONH region. (c) Sagittal view of the ONH region. The red line indicates a section through the lamina cribrosa obtained for the comparison of fiber orientation with SPLM on the remaining thick tissue.

the fiber retardance and orientation.⁹ For both fixed and fresh eyes, we hemisected the globe and retained the posterior portion. The top view of the posterior pole and the typical anatomy of the eye is shown in Figs. 1(a) and 1(b), respectively. The retina and most superficial prelaminar tissues were carefully removed while under the microscope to ensure that the laminar connective tissues were not disrupted. Afterward, the ONH and peripapillary sclera region were excised using a 16-mm diameter trephine [dashed-circle in Fig. 1(a)]. The ONH is located in the back of the eye, where retinal ganglion cell axons converge and exit the eye through a mesh-like collagenous structure called lamina cribrosa. Both collagen beams and neural tissues are highly scattering, and previous studies have shown that collagen beams are more scattering than neural tissues.²³ The neural tissues appear to have similar properties to white matter, which has weak absorption and the collagen tissues were also reported to have weak absorption.^{24,25} To compare the performance of SPLM on thick tissues with regular PLM on thin sections, we fixed and cryosectioned coronally (transversely) a sheep ONH starting from the anterior side. After each 25- μm -thick section was placed on the glass slide, it was inspected under the microscope. As soon as a good section through the lamina cribrosa was obtained, the cryosectioning was stopped (Fig. 1). The comparison was thus made between PLM on the last cryosection collected and SPLM of the remaining thick ONH. The thick ONH was placed in a custom inflation chamber for imaging [Fig. 2(a)]. The custom chamber allowed clamping the peripheral sclera and controlling pressure using a column filled with phosphate-buffered saline (PBS) (not shown).

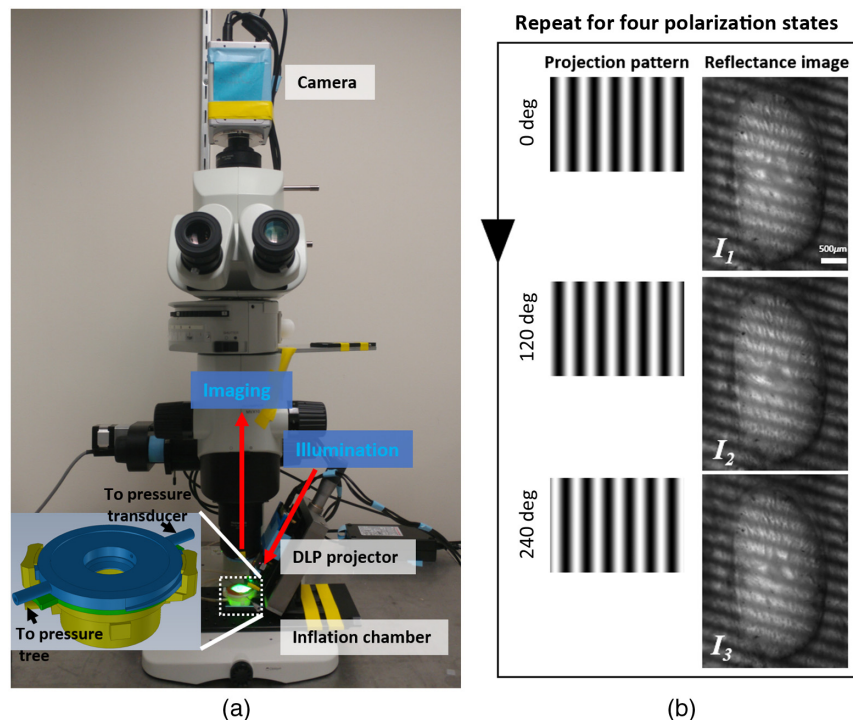


Fig. 2 (a) SPLM configuration based on an upright microscope. A DLP projector generates and projects patterns onto a sample placed in an inflation chamber (enlarged view in the inset). A CMOS camera captures reflectance images. (b) Example of projected patterns shifted at three phases (left column) and corresponding reflectance images of the sample (right column).

2.2 Imaging and Analysis

We developed an SPLM imaging system, as shown in Fig. 2(a), based on a commercial upright microscope (MVX10, Olympus, Tokyo, Japan). The microscope features a variable magnification control with a zoom ratio of 1:10 (0.63× to 6.3×). The structured light illumination was achieved with a digital light projector (DLP) (LightCrafter evaluation module, Texas Instruments, Dallas). The projection axis was set to 30 deg off the imaging axis. A circular polarizer and a rotating linear polarizer were placed in front of the projection lens and the imaging objective, respectively. The illumination was filtered with a bandpass filter centered at 535 nm with a pass-band of 64.4 nm (IF 550, Olympus, Tokyo, Japan). The illumination was filtered with a bandpass filter centered at 535 nm with a passband of 64.4 nm (IF 550, Olympus, Tokyo, Japan). Elsewhere, we have demonstrated the use of 535-nm green illumination and polarization filters for accurate fiber orientation quantification.⁹ In principle, other wavelengths could be equally useful. In preliminary tests (results not shown), we evaluated other wavelengths, and obtained the best results with 535 nm. To perform polarization-sensitive imaging, the linear polarizer was rotated sequentially to four polarization angles: 0 deg, 45 deg, 90 deg, and 135 deg. At each polarization state, three two-dimensional (2-D) sinusoidal patterns with a phase shift of 0 deg, 120 deg, and 240 deg were sequentially projected onto the sample [left column, Fig. 2(b)]. The corresponding reflectance images, I_1 , I_2 , and I_3 , were acquired by a COMS camera (ORCA-Flash4.0 LT, Hamamatsu, Hamamatsu City, Japan) [Fig. 2(b)]. An effective 4× magnification was achieved with the combination of a 1× objective (MVPLAPO 0.25NA, Olympus, Tokyo, Japan) and a 4× optical zoom. The spatial frequency used in the imaging was 3 mm⁻¹. Both pattern projection and image acquisition were controlled by a custom LabVIEW program:

$$I_{DC} = \frac{1}{3}(I_1 + I_2 + I_3), \quad (1)$$

$$I_{AC} = \frac{\sqrt{2}}{3} \left[\sqrt{(I_1 - I_2)^2 + (I_2 - I_3)^2 + (I_3 - I_1)^2} \right]. \quad (2)$$

At each polarization state, two images, I_{DC} and I_{AC} , were derived with the demodulation process shown in Eqs. (1) and (2).²⁶ The DC image is equivalent to the reflectance image under planar illumination, whereas the AC image is the image with the diffuse background suppressed. Both AC and DC images at the four polarization states can be used to compute a regular reflectance image (AC or DC) by taking an average of the intensity images at two orthogonal polarization states, e.g., $I_{0 \text{ deg}}$ and $I_{90 \text{ deg}}$, and a fiber orientation map as previously described.⁹

The thin section was imaged with an inverted microscope (IX83, Olympus, Tokyo, Japan) with a strain-free 4× objective using the regular PLM technique that we previously reported.⁹ Essentially, the imaging procedure and the analysis of PLM are the same as the one described above for SPLM except using non-SLI transmitted light.

2.3 SPLM imaging of Optic Nerve Head

2.3.1 SPLM imaging under zero pressure

Both fixed sheep and fresh pig ONH tissues were imaged with the SPLM imaging system. The thick ONH samples were

submerged in PBS and no pressure was applied during imaging. We obtained collagen fiber structure and orientation images with (AC-based analysis) and without SPLM analysis (DC-based analysis). The 25-μm-thick sheep ONH section was rehydrated with PBS, coverslipped, and imaged using regular PLM. To demonstrate the improvement brought about by SPLM, the visibility and contrast of collagen beams and the accuracy of collagen fiber orientation were assessed in collagen fiber structure and orientation images.

2.3.2 SPLM imaging during inflation test

To demonstrate the potential of SPLM for biomechanical studies, we conducted SPLM imaging of a fresh pig ONH during an inflation test. The trephined posterior ONH portion was carefully mounted inside the pressure chamber to ensure that the lamina cribrosa was centered in the field of view. The 16-mm diameter of the sample provides realistic boundary conditions for the ONH and lamina cribrosa within.²⁷ The anterior chamber is connected to a PBS column with an in-line pressure transducer to monitor the induced intraocular pressure. The pressure was increased from 5 to 50 mmHg in increments of 5 mmHg. After each increase in pressure, we waited 15 min before taking measurements to allow tissue viscoelastic effects to dissipate.²⁸ On the images from each pressure, we manually delineated the sclera canal and measured the lengths of long and short axes of the canal, D_L and D_S , respectively. Further, we quantified the canal size, the aspect ratio ($= D_L/D_S$) as well as local fiber orientation changes along the pressure ramp.

3 Results

3.1 SPLM Imaging under Zero Pressure

3.1.1 Collagen fiber structures

The DC and AC images of fixed sheep ONH are shown in Figs. 3(a) and 3(b), respectively. Both collagen beams and neural tissues are visible in the DC image, but the contrast between them is low. In comparison, the AC image shows much-improved contrast and visibility of collagen beams, with the neural tissue region mostly dark. A closer look at a region-of-interest (ROI), indicated with a green-dashed box in the DC [Fig. 3(d)] image and red-dashed box in the AC image [Fig. 3(c)], allows distinguishing more collagen beams in the AC image than in the DC image. The improved visibility can be evaluated quantitatively by plotting an intensity profile along a line ROI. Comparing the profiles in the DC and AC images [Fig. 3(g)] revealed an improvement almost 10-fold in the contrast, computed as the ratio of the intensity range over the minimum intensity, from 0.056 in the DC image to 0.54 in the AC image. This contrast improvement allows detecting more collagen beams in the AC image, such as the one indicated by the red arrow. The contrast improvement in the AC image was also observed in the sclera region [brown box in (a) and blue box in (b)] outside the canal, where tissues had smaller variations in the scattering than in the lamina cribrosa. Nevertheless, collagen bundles exhibited better visibility in the AC image [Fig. 3(e)] than in the DC image [Fig. 3(f)]. Line intensity profiles [Fig. 3(h)] confirmed that intensity variations from collagen undulations, or crimp, were more easily discerned in the AC image than in the DC image. Furthermore, the effect of pigment absorption is greatly reduced in the AC image. The reduction of this effect can be seen clearly when

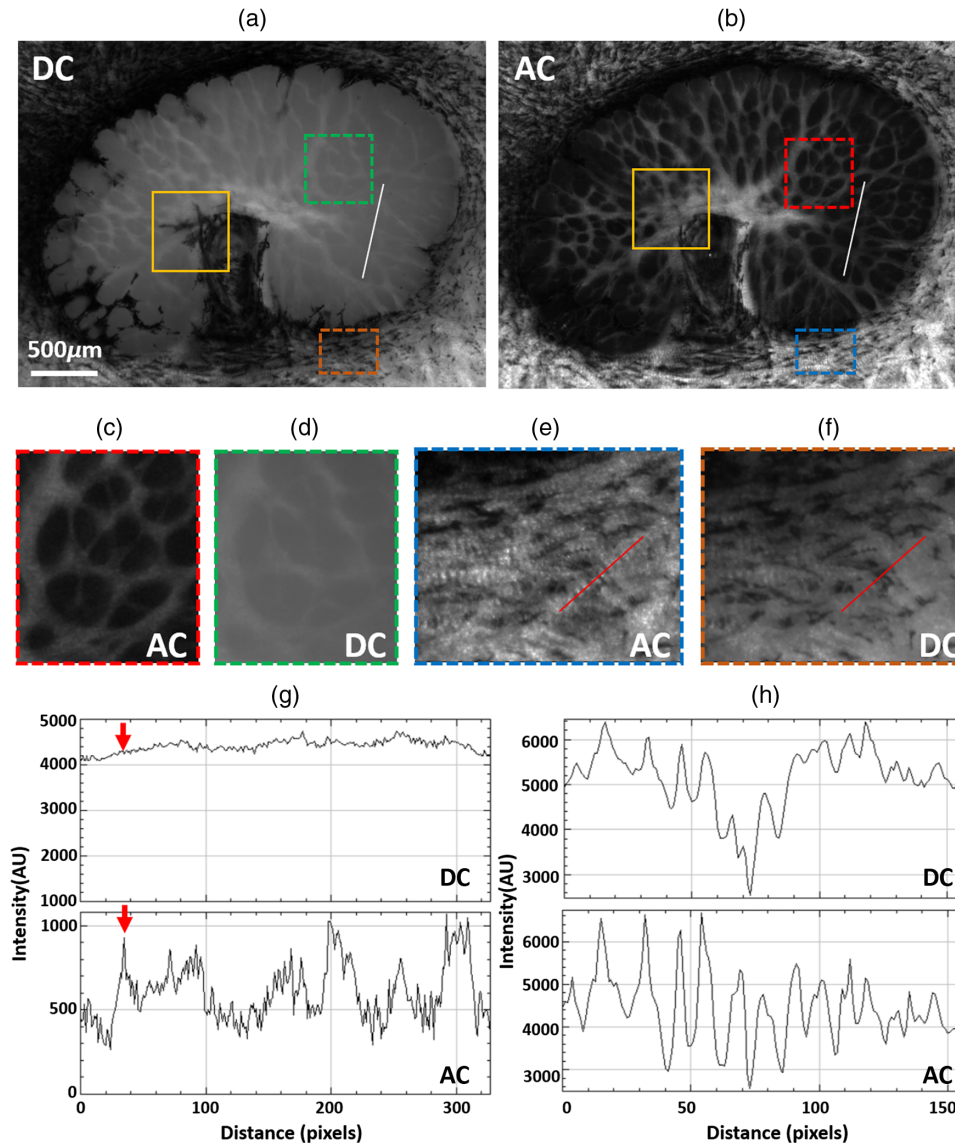


Fig. 3 (a) DC and (b) AC images of a fixed sheep ONH. The AC image shows improved visibility and contrast of collagen beams. The ROI indicated with a yellow box shows less pigment absorption in AC image than in DC image. Close-up images, (c) and (d), of the ROIs indicated with red and green dotted-box in (b) and (a), respectively. (e) and (f) Close-up images of two ROIs in sclera regions indicated with brown and blue dotted-box in (a) and (b), respectively. (g) Intensity profiles over the same line ROI in both DC and AC images. The red arrow illustrates that the AC image allows detecting more collagen beam than the DC image. (h) Intensity profiles over the line ROIs in both (e) and (f). The AC intensity profile shows more regular intensity variation along a collagen beam.

comparing the region in the yellow boxes in Figs. 3(a) and 3(b). Although pigment obscures the beams quite substantially in DC, the beam structure is visible in the AC image.

Improvements in collagen visibility can also be observed in the fresh pig ONH images shown in Fig. 4. Compared with sheep ONH, pig ONH has a denser collagen beam network and thinner beams. The DC image shows very poor visibility of collagen beams with only large beams visible. Smaller beams are almost masked by the scattered light from neural tissues. By rejecting the diffuse signal from neural tissues, the AC image shows many more thin beams with a substantially improved contrast. Two vessel openings indicated with two yellow arrows, almost impossible to recognize in the DC, become well contrasted. Close-up views of the ROIs, indicated with red and green boxes in Fig. 4(b), show the level of details in the AC

image [Figs. 4(c) and 4(d)]. Not only can small beams be seen in Fig. 4(c) but also the alternating intensity-varying bands along the beam, which is known as crimp, an important characteristic of the collagen fibers.¹² Different morphologies of collagen beams in Figs. 4(c) and 4(d) can also be observed: in Fig. 4(c) beams appear flat, whereas in Fig. 4(d) they vary in intensity, in what appears consistent with their “tubular” shape.

3.1.2 Collagen fiber orientation mapping

Figure 5 shows the collagen fiber orientation maps of both thick sheep ONH [Figs. 5(a) and 5(b)] and thin ONH section [Fig. 5(c)]. The collagen fiber orientation maps in Figs. 5(a) and 5(b) were obtained without and with SPLM, e.g., analyzed with DC images and AC images, respectively. By comparing

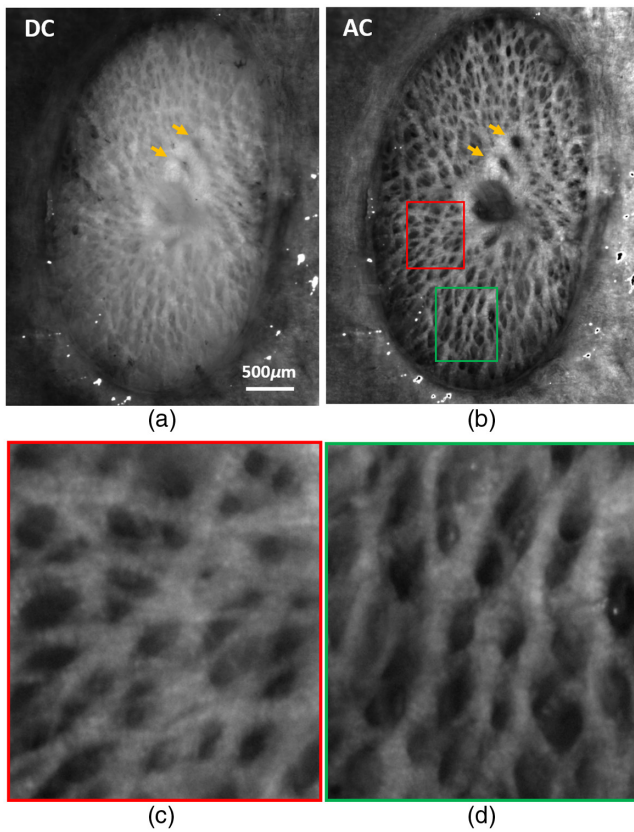


Fig. 4 (a) DC and (b) AC images of a fresh pig ONH. AC images shows much-improved visibility and contrast of collagen beams and of the blood vessels indicated with yellow arrows. (c) and (d) Close-up images of the ROIs indicated with red and green boxes in (d).

two orientation maps, it is evident that with SPLM, collagen beams are better defined with reduced background, e.g., signals from neural tissues. Orientation lines, computed as described elsewhere,⁹ followed the collagen beams very well [Fig. 5(e)]. Without SPLM, in thick tissues, orientation lines deviated from the fiber beams, which we have shown is most likely incorrect. The fiber orientation map of the thick ONH obtained with SPLM is very similar, but not identical, to the orientation map of the immediately adjacent thin section imaged with PLM, as should be expected. The collagen beams appear slightly narrower in the PLM images of the cryosection than in the SPLM images of the thick sample. The mean and standard deviation of collagen fiber orientations in the three regions indicated with the yellow boxes in Figs. 5(d)–5(f) were $-4.1 \text{ deg} \pm 6.7 \text{ deg}$, $15.8 \text{ deg} \pm 3.2 \text{ deg}$, and $-2.7 \text{ deg} \pm 2.9 \text{ deg}$, respectively. Fiber orientation distribution obtained with SPLM had the same mode and similar shape compared with the distribution obtained from a thin section imaged using regular PLM. Without SPLM, the mean fiber orientation deviated about 20 deg from the reference direction obtained with regular PLM.

The collagen fiber orientation maps of pig ONH derived with and without SPLM are shown in Figs. 6(a) and 6(b), respectively. Although the two orientation maps show very similar colors, upon closer examination, it can be discerned that the orientation maps from SPLM follow the structure more closely. Figure 6(c) shows fiber orientation lines in a close-up of the white ROI shown in Fig. 6(a). Without referring to the fiber structure image, it is almost impossible to reliably distinguish

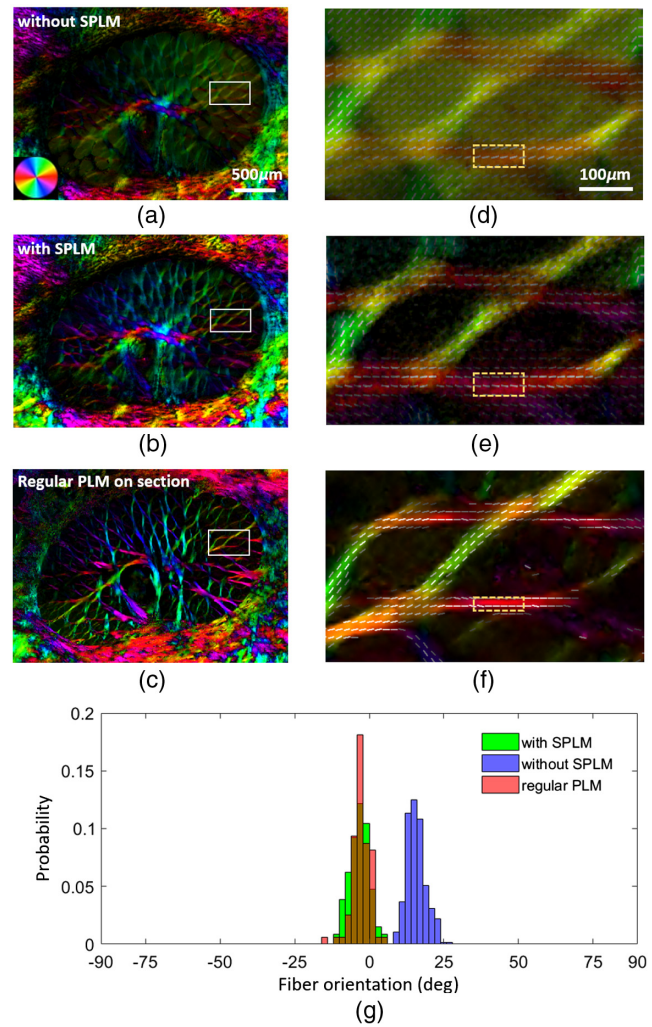


Fig. 5 The panels show fiber orientation maps of thick fresh sheep ONH obtained (a and d) without SPLM, (b and e) with SPLM, (c and f) of a 25-μm-thick section obtained using regular PLM, and the histograms of fiber orientations of the three ROIs indicated with yellow boxes in (d), (e), and (f). The colors in the fiber orientation images correspond to the fiber orientation as per the legend shown in the bottom-left of (a). The left-side column shows full views of the lamina cribrosa, whereas the right-side column shows close-ups of the ROIs indicated with the white boxes on the left-hand-side images. In addition to the good contrast, orientations derived from SPLM show excellent agreement with those from PLM. Orientations obtained without SPLM deviated by about 20°.

collagen beams from neural tissues. The light scattering resulted in artifactual fibers within the lamina pores. With SPLM, in Fig. 6(d), collagen beams are well defined. The collagen beams can be easily followed by tracing orientation lines. The histograms in Fig. 6(e) show two distributions of orientations within two ROIs of a beam indicated by red boxes in Figs. 6(c) and 6(d), respectively. The mean and standard deviation of fiber orientations in the two beam ROIs are $69.2 \text{ deg} \pm 4.0 \text{ deg}$ with SPLM and $60.1 \text{ deg} \pm 8.0 \text{ deg}$ without SPLM. Although the histogram without SPLM shows a narrower shape compared with the one with SPLM, the latter follows the beam better and captures the fiber turning from large angles to smaller angles. The apparent collagen beam orientation measured with FIJI²⁹ was 54.6 deg and is indicated with a dashed-blue line in Fig. 6(e). The fiber orientation obtained with SPLM had

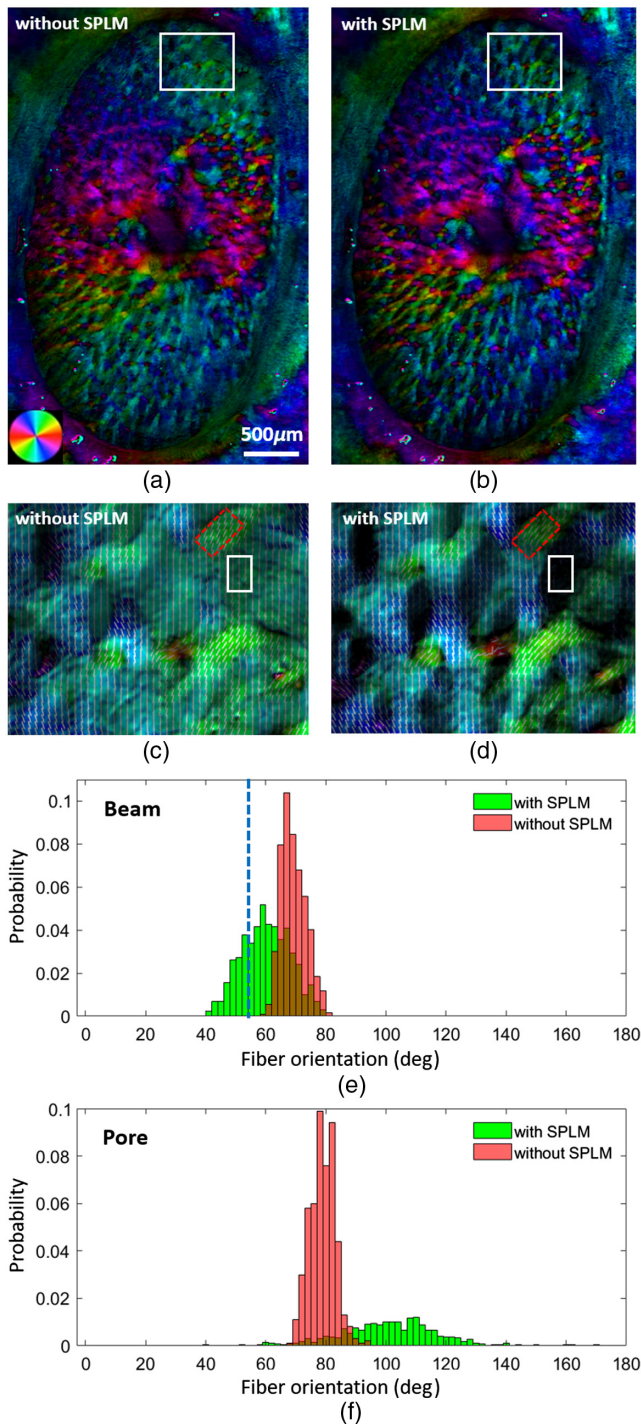


Fig. 6 (a) and (b) Collagen fiber orientation maps of a fresh pig ONH obtained without and with SPLM, respectively. (c) and (d) Close-up orientation images obtained without and with SPLM, respectively, of the ROI indicated with a white box in (a). (d) A much-improved collagen beam definition in the images obtained using SPLM. (e) The histogram of fiber orientation of the two ROIs indicated with red boxes in (c) and (d). The blue dashed-line indicates the apparent orientation of the collagen beam measured manually. (f) The energy-weighted histogram of the fiber orientation in the pore indicated with a white box. Orientations measured with SPLM (and with energy weighting in the pore) were in better agreement with the expectations.

a good agreement with the apparent collagen beam orientation. Figure 6(f) shows energy-weighted histograms of the fiber orientation in the pore. The energy measurement is directly related to the retardance.⁹ Without SPLM, the neural tissue in the pore exhibited a strong directionality with high visibility, which is likely artifactual considering the known organization and properties of the neural tissues in the lamina cribrosa.³⁰ With SPLM, however, the energy properly scaled down the visibility of the calculated orientation, thus allowing more specific and more accurate visualization of collagen fiber orientation.

3.2 SPLM Imaging during the Inflation Test

Figure 7(a) shows an example of an image of a fresh pig ONH mounted in the inflation chamber, with the scleral canal segmented. The red line indicates the canal region and white double-arrows show both short and long axes of the canal. As the pressure increased from 5 to 50 mmHg, the size of the canal increased by 15% from 3.13 to 3.60 mm². It was found that canal expansion underwent two general stages [Fig. 7(b)]: the canal expanded more under low pressures (<20 mmHg) and less under high pressures (>20 mmHg). This observation is consistent with the nonlinear material properties of collagenous tissues. It was noted that although the canal expanded, the aspect ratio remained approximately unchanged at 1.842 over 10 pressures. The white box in Fig. 7(a) shows a collagen beam and the inset shows the close-up of that beam with a dotted-line ROI. This ROI was used to track the fiber orientation across inflation pressures as shown in Fig. 7(c), where at each pressure, the average (dots) and standard deviations (error bars) of the orientation were plotted. The average fiber orientation decreased by 15 deg from 90 deg to ~75 deg as the pressure increased from 5 to 20 mmHg, indicating a rotational deformation. The fiber orientation of the collagen beam then remained constant around 75 deg for the rest of pressures.

4 Discussion

We demonstrated that SPLM is an effective and robust method for visualizing and quantifying collagen fiber properties of thick ocular tissues. By utilizing SLI with PLM, the collagen fiber structure images showed a significantly improved contrast between collagen beams and neural tissues, as well as reduced pigment absorption effects. This improved visualization and allowed detecting more lamina cribrosa beams than without SLI. Furthermore, the fiber orientation maps made with SPLM were more accurate. Finally, we demonstrated that SPLM is a valuable tool for direct visualization and tracking of ONH deformation when integrated with an inflation device.

The improvements achieved with SPLM are twofold: (1) “optical removal” of neural tissues around collagen beams and (2) suppression of multiple scattered light. Optical removal can be done because of the lower scattering of neural tissues relative to collagen. Under the structured light illumination, the collagen beams preserve the structured illumination modulation (peak-to-valley of the illumination pattern) better than the neural tissue does. In other words, the modulation is attenuated much faster in neural tissues, resulting in very small modulation detected in the neural tissue region, which results in very small signal intensity after the demodulation processing. This is the effect we refer to as optical removal of neural tissues. As a result, the visibility of collagen beams is greatly enhanced.

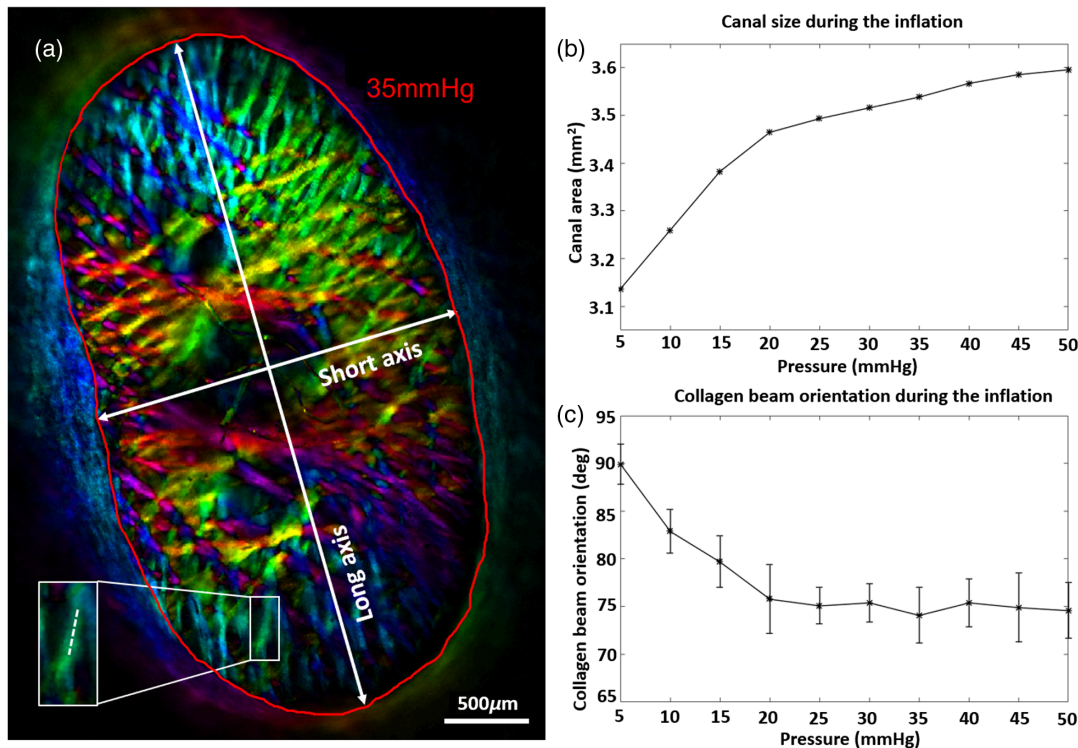


Fig. 7 (a) Fiber orientation map of a fresh pig ONH at 35 mmHg intraocular pressure. Double-arrows indicate short and long axes of the scleral canal. The red line indicates the manual segmentation of the scleral canal, enclosing the lamina cribrosa. (b) Canal size as a function of inflation pressure. (c) Collagen beam orientation as a function of inflation pressure. The collagen beam was indicated with a white box in (a). The error bar indicates the standard deviation of fiber orientation. The inset shows the close-up image of the collagen beam and the mean and standard deviation of the fiber orientation were calculated along the dotted-line.

The second improvement using SPLM was the suppression of the multiple scattered light. As the polarized light propagates into the biological tissue, it interacts with tissues via birefringence and scattering. The tissue birefringence alters the polarization states of the illumination, and the reflected light carries the information about the tissue structure. The multiple scattering events compromise the polarization integrity of the reflected light by introducing scattered light from surrounding collagen and neural tissues. Using the polarization state of multiple scattered light to determine fiber orientations could lead to errors, as has been demonstrated in Sec. 3.1.2. However, the multiple scattering also reduces the modulation of the SLI, and therefore its potentially artifactual signal can be effectively reduced by the demodulation process. Compared with regular reflectance images or DC images, AC images highlight useful polarization changes from collagen fibers with little contribution from multiple scattering, which leads to more accurate quantification of collagen fiber orientation.

Studying tissue response under controlled loadings is a crucial step toward investigating mechanical properties of ocular tissues.^{31–34} Ocular biomechanics have been studied, for example, using scanning light scattering techniques, such as small angle light scattering (SALS)³⁵ and wide-angle x-ray scattering (WAXS).²⁷ However, these techniques are limited in that they provide fiber orientation information averaged across the depth of thick tissues. In addition, the spatial resolution is not high enough to resolve individual collagen beams in the lamina cribrosa.³⁵ Another imaging technique often used to study the eye is second harmonic generation (SHG). SHG is highly

specific and sensitive, providing high-resolution visualization of the collagen structures without exogenous labeling.^{16,36–38} The nonlinear nature of SHG enables optical sectioning and with lower phototoxicity risk than traditional confocal imaging.¹⁸ This is particularly advantageous in thick tissues. Because of these strengths, SHG has been applied to the study of lamina cribrosa structure and biomechanics.^{16,38–40} Despite the success, SHG also has important limitations, for instance, high resolution and wide field of view can only be achieved at the expense of a substantially longer imaging time, which restricts the type of possible studies. ONH and lamina cribrosa biomechanics are also often studied using optical coherence tomography, which has the important advantage that it can be used *in vivo*.^{1,41,42} However, despite exciting advances, such as the integration of polarized light information,^{43,44} the light-penetration, resolution, and contrast of these systems are not yet sufficient to quantitatively analyze lamina cribrosa beams with the level of detail demonstrated with SPLM in this work. A study using serial sectioning of eyes fixed at various intraocular pressures followed by PLM imaging has addressed some of these issues, and indeed provided valuable findings.²⁰ However, individual collagen beams of the ONH could not be tracked with pressure. This need for multiple eyes (one at each pressure) increased both experimental complexity and variability of the measurements. While the results were encouraging, they are very time consuming and have low sensitivity to detect effects of small pressure changes.

SPLM imaging has advantages that make it an excellent for deformation visualization and tracking in biomechanical

testing studies of the lamina cribrosa. SPLM imaging provides both high-resolution and wide-field imaging capabilities, which allows the visualization of individual collagen beams in ONH and peripapillary sclera without scanning. As a reflected light imaging technique, SPLM can be used to image a variety of thick tissues with minimal tissue processing, which preserves the tissues' intrinsic mechanical properties, a critical prerequisite for mechanical testing of biological samples. Further, SPLM imaging can be very fast (<100 ms for a full-field image) when paired with an advanced polarization sensitive camera,⁴⁵ which will allow for time-sensitive deformation measurements.

This study is not the first to use SLI to reduce scattering effects and improve the accuracy of collagen fiber orientation mapping on thick tissues. Yang and colleagues first introduced this use of SLI for heart valve imaging with polarized light spatial frequency-domain imaging (pSFDI) in 2015.⁴⁶ Compared with their original method, the SPLM presented here has several advantages. SPLM requires only four images to derive fiber orientations, as opposed to 18 images, or more, required by pSFDI. SPLM uses a higher spatial frequency of 3 mm^{-1} compared with 1 mm^{-1} in pSFDI, which permits more effective diffuse background rejection and higher accuracy of orientation quantification. The choice of the spatial frequency at 3 mm^{-1} was based on the following considerations: a higher spatial frequency is more effective in rejecting diffuse light. However, if the spatial frequency is too high, the demodulated signal will be small, with reduced signal-to-noise ratio, thus adversely affecting the analysis. In a preliminary study (not shown), we found that the spatial frequency at 3 mm^{-1} provided good background rejection while still maintaining good signal-to-noise ratio for the analysis. Furthermore, projecting with a spatial frequency of 3 mm^{-1} also satisfied other system requirements, such as allowing sufficient working distance for the inflation device.

Wavelength has been used to control imaging depth, with a shorter wavelength yielding a shallower imaging depth.⁴⁷ To image the superficial layer of the tissue, a wavelength such as 275 nm in the UV range could be used.⁴⁸ However, UV illumination causes several problems, including potentially harmful ionizing effects and increased system configuration complexity. Compared with wavelength-dependent probing depth, SLI with visible light offers a greater flexibility on controlling the probing depth by adjusting the spatial frequency of the illumination. Under planar illumination, the imaging depth is dependent on the optical properties of the tissue, which are themselves dependent on the wavelength. The imaging depth can be described as $d = \{\sqrt{3\mu_a(\lambda)[\mu_a(\lambda) + \mu'_s(\lambda)]}\}^{-1}$, where μ_a , μ'_s , and λ are absorption coefficient, reduced scattering coefficient, and wavelength, respectively.²⁶ Under structured illumination, the imaging depth is further dependent on the spatial frequency and can be described as $d = \{\sqrt{3\mu_a(\lambda)[\mu_a(\lambda) + \mu'_s(\lambda)] + (2\pi f)^2}\}^{-1}$, which offers a much greater tuning range of the imaging depth compared with using planar illumination.²⁶ The imaging depth can be tuned over a wide range of the spectrum. SLI can be easily integrated into our existing imaging system without complex reconfiguration. At higher spatial frequency, the imaging depth can be estimated as $d \approx (2\pi f)^{-1}$.²⁶ In this study, the imaging depth was estimated as $53 \mu\text{m}$ at $f = 3 \text{ mm}^{-1}$.

It is worth noting that although we demonstrated SPLM imaging with thick ocular tissues with large spatial differences in scattering, the technique will potentially work well on nonocular thick soft collagenous tissues as the underlying principle still

applies. For tissues with smaller variations in scattering, the contrast improvement may not be as substantial as the one presented in this study. However, the demodulated image should still appear sharper and better contrasted with the rejection of diffuse background as we demonstrated in Figs. 3(e) and 3(h). Unlike the contrast enhancement, the improvement of the quantification accuracy of collagen fiber orientation is not dependent on the scattering variation. In the other words, the quantification accuracy improvement should be similar for tissues both with and without large spatial scattering variations.

Although these two studies focused on collagen fiber orientation mapping of thick tissues, SLI can be considered as a general illumination strategy to improve accuracy in thick tissue polarimetry, such as full Mueller matrix imaging.⁴⁹ Mueller matrix imaging can quantitatively evaluate the polarization and depolarization properties of the tissue,⁵⁰ with potential clinical diagnostic applications.⁴⁷ Integrating SLI with Mueller polarimetry has the potential to image tissues over a wide range of the spectrum while still maintaining the imaging depth control. Use of SLI does not preclude a depolarization study. The modulation of SLI decreases as it propagates into the tissue due to the scattering. The demodulation analysis rejects highly diffused signal with little modulation from the deep tissues, but preserves the signal maintaining a decreased but detectable modulation. In other words, within the imaged depth, the scattering also exists and introduces some depolarization, which can be further investigated.

This study is an initial demonstration of how SPLM can be integrated with an inflation device to perform direct visualization and deformation tracking in an inflation test of a fresh pig ONH. The quantification of canal deformation and fiber orientation change is intended as a proof of principle for how integrating SPLM imaging could benefit biomechanical studies of ocular tissues. The tissue deformation information can further be studied using advanced analysis techniques such as quantifying material properties using inverse finite-element modeling⁵¹ and quantifying deformation using digital image correlation.^{16,52} The high contrast provided by SPLM suggests that tracking and quantifying deformations using digital image correlation would not require placing markers or adding exogenous contrast agents. In addition to simplifying the experimental setup, this will allow tracking over the entire visible region, instead of only the regions with good markers. An important future direction of SPLM is to capture the deformations in three-dimensional (3-D). The SPLM used in this study captured collagen fiber properties in 2-D. During mechanical testing, the tissue likely deforms in a 3-D space. Although previous studies have suggested that using the analysis with 2-D deformation data may be sufficient for certain studies,^{19,39} capturing the deformation in 3-D would be more accurate. Future studies could incorporate 3-D tissue tracking using techniques such as stereoscopic depth tracking or perhaps utilizing 3-D information of the fibers.¹⁰

5 Conclusion

We demonstrated that SPLM is a robust imaging technique for visualization and quantification of collagen fiber structure and orientation in thick ocular tissues. When integrated with a mechanical testing device, SPLM provides direct structure visualization and deformation tracking of collagen structures, which facilitate ocular biomechanical studies. SPLM, although demonstrated for the applications in ocular tissues, can be

extended to other types of thick collagenous tissues, e.g., heart valve tissues.

Disclosures

We have no proprietary interests or conflicts of interests to disclose.

Acknowledgments

This research work was supported, in part, by grants from National Institutes of Health under Grant Nos. NIH R01-EY023966, R01-EY025011, R01-EY028662, T32-EY017271, and P30-EY008098, Eye and Ear Foundation (Pittsburgh, PA) and Research to prevent blindness (support to the UPMC Department of Ophthalmology). Part of the work in this study was presented at SPIE Photonics West 2018.⁵³

References

- Z. Nadler et al., "In vivo three-dimensional characterization of the healthy human lamina cribrosa with adaptive optics spectral-domain optical coherence tomography," *Invest. Ophthalmol. Visual Sci.* **55**(10), 6459–6466 (2014).
- K. M. Meek and C. Knupp, "Corneal structure and transparency," *Prog. Retinal Eye Res.* **49**, 1–16 (2015).
- J. K. Pijanka et al., "Quantitative mapping of collagen fiber orientation in non-glaucoma and glaucoma posterior human sclera/fiber orientation in posterior human sclera," *Invest. Ophthalmol. Visual Sci.* **53**(9), 5258–5270 (2012).
- B. Coudrillier et al., "Effects of peripapillary scleral stiffening on the deformation of the lamina cribrosa," *Invest. Ophthalmol. Visual Sci.* **57**(6), 2666–2677 (2016).
- N. A. McBrien, L. M. Cornell, and A. Gentle, "Structural and ultrastructural changes to the sclera in a mammalian model of high myopia," *Invest. Ophthalmol. Visual Sci.* **42**(10), 2179–2187 (2001).
- A. Caporossi et al., "Parasurgical therapy for keratoconus by riboflavin-ultraviolet type A rays induced cross-linking of corneal collagen: preliminary refractive results in an Italian study," *J. Cataract Refractive Surg.* **32**(5), 837–845 (2006).
- G. Wollensak, E. Spoerl, and T. Seiler, "Riboflavin/ultraviolet-A-induced collagen crosslinking for the treatment of keratoconus," *Am. J. Ophthalmol.* **135**(5), 620–627 (2003).
- N.-J. Jan, K. Lathrop, and I. A. Sigal, "Collagen architecture of the posterior pole: high-resolution wide field of view visualization and analysis using polarized light microscopy," *Invest. Ophthalmol. Visual Sci.* **58**(2), 735–744 (2017).
- N.-J. Jan et al., "Polarization microscopy for characterizing fiber orientation of ocular tissues," *Biomed. Opt. Express* **6**(12), 4705–4718 (2015).
- B. Yang et al., "Polarized light microscopy for 3-dimensional mapping of collagen fiber architecture in ocular tissues," *J. Biophotonics* **11**(8), e201700356 (2018).
- N.-J. Jan et al., "Microstructural crimp of the lamina cribrosa and peripapillary sclera collagen fibers," *Invest. Ophthalmol. Visual Sci.* **58**(9), 3378–3388 (2017).
- N.-J. Jan et al., "Crimp around the globe: patterns of collagen crimp across the corneoscleral shell," *Exp. Eye Res.* **172**, 159–170 (2018).
- A. Gogola et al., "Spatial patterns and age-related changes of the collagen crimp in the human cornea and sclera," *Invest. Ophthalmol. Visual Sci.* **59**(7), 2987–2998 (2018).
- B. C. Perez et al., "Mapping 3D strains with ultrasound speckle tracking: method validation and initial results in porcine scleral inflation," *Ann. Biomed. Eng.* **44**(7), 2302–2312 (2016).
- B. Coudrillier et al., "Biomechanics of the human posterior sclera: age-and glaucoma-related changes measured using inflation testing," *Invest. Ophthalmol. Visual Sci.* **53**(4), 1714–1728 (2012).
- I. A. Sigal et al., "Eye-specific IOP-induced displacements and deformations of human lamina cribrosa," *Invest. Ophthalmol. Visual Sci.* **55**(1), 1–15 (2014).
- S. Alali and I. A. Vitkin, "Polarized light imaging in biomedicine: emerging Mueller matrix methodologies for bulk tissue assessment," *J. Biomed. Opt.* **20**(6), 061104 (2015).
- P. J. Campagnola and L. M. Loew, "Second-harmonic imaging microscopy for visualizing biomolecular arrays in cells, tissues and organisms," *Nat. Biotechnol.* **21**(11), 1356–1360 (2003).
- B. Coudrillier et al., "Phase-contrast micro-computed tomography measurements of the intraocular pressure-induced deformation of the porcine lamina cribrosa," *IEEE Trans. Med. Imaging* **35**(4), 988–999 (2016).
- N.-J. Jan and I. A. Sigal, "Collagen fiber recruitment: a microstructural basis for the nonlinear response of the posterior pole of the eye to increases in intraocular pressure," *Acta Biomater.* **72**, 295–305 (2018).
- N. Fatehee et al., "Correlating morphometric parameters of the porcine optic nerve head in spectral domain optical coherence tomography with histological sections," *Br. J. Ophthalmol.* **95**(4), 585–589 (2011).
- H. Tran et al., "Formalin fixation and cryosectioning cause only minimal changes in shape or size of ocular tissues," *Sci. Rep.* **7**(1), 12065 (2017).
- D. Kasaragod et al., "Machine-learning based segmentation of the optic nerve head using multi-contrast Jones matrix optical coherence tomography with semi-automatic training dataset generation," *Biomed. Opt. Express* **9**(7), 3220–3243 (2018).
- S. K. V. Sekar et al., "Diffuse optical characterization of collagen absorption from 500 to 1700 nm," *J. Biomed. Opt.* **22**(1), 015006 (2017).
- A. Yaroslavsky et al., "Optical properties of selected native and coagulated human brain tissues in vitro in the visible and near infrared spectral range," *Phys. Med. Biol.* **47**(12), 2059–2073 (2002).
- B. Yang and J. W. Tunnell, "Real-time absorption reduced surface fluorescence imaging," *J. Biomed. Opt.* **19**(9), 090505 (2014).
- B. Coudrillier et al., "Scleral anisotropy and its effects on the mechanical response of the optic nerve head," *Biomech. Model. Mechanobiol.* **12**(5), 941–963 (2013).
- I. A. Sigal et al., "Reconstruction of human optic nerve heads for finite element modeling," *Technol. Health Care* **13**(4), 313–329 (2005).
- J. Schindelin et al., "Fiji: an open-source platform for biological-image analysis," *Nat. Methods* **9**(7), 676–682 (2012).
- C. Balaratnasingam et al., "Axonal transport and cytoskeletal changes in the laminar regions after elevated intraocular pressure," *Invest. Ophthalmol. Visual Sci.* **48**(8), 3632–3644 (2007).
- T. D. Nguyen and C. R. Ethier, "Biomechanical assessment in models of glaucomatous optic neuropathy," *Exp. Eye Res.* **141**, 125–138 (2015).
- I. A. Sigal et al., "Modeling individual-specific human optic nerve head biomechanics. Part I: IOP-induced deformations and influence of geometry," *Biomech. Model. Mechanobiol.* **8**(2), 85–98 (2009).
- I. A. Sigal et al., "Modeling individual-specific human optic nerve head biomechanics. Part II: influence of material properties," *Biomech. Model. Mechanobiol.* **8**(2), 99–109 (2009).
- I. C. Campbell, B. Coudrillier, and C. R. Ethier, "Biomechanics of the posterior eye: a critical role in health and disease," *J. Biomech. Eng.* **136**(2), 021005 (2014).
- M. J. Girard et al., "Quantitative mapping of scleral fiber orientation in normal rat eyes," *Invest. Ophthalmol. Visual Sci.* **52**(13), 9684–9693 (2011).
- M. Han, G. Giese, and J. F. Bille, "Second harmonic generation imaging of collagen fibrils in cornea and sclera," *Opt. Express* **13**(15), 5791–5797 (2005).
- D. J. Brown et al., "Application of second harmonic imaging microscopy to assess structural changes in optic nerve head structure ex vivo," *J. Biomed. Opt.* **12**(2), 024029 (2007).
- S. Ram et al., "Three-dimensional segmentation of the ex-vivo anterior lamina cribrosa from second-harmonic imaging microscopy," *IEEE Trans. Biomed. Eng.* **65**(7), 1617–1629 (2018).
- D. E. Midgett et al., "The pressure-induced deformation response of the human lamina cribrosa: analysis of regional variations," *Acta Biomater.* **53**, 123–139 (2017).
- H. Jones et al., "Quantitative analysis of three-dimensional fibrillar collagen microstructure within the normal, aged and glaucomatous human optic nerve head," *J. R. Soc. Interface* **12**(106), 20150066–20150066 (2015).
- I. A. Sigal et al., "Recent advances in OCT imaging of the lamina cribrosa," *Br. J. Ophthalmol.* **98**(Suppl. 2), ii34–ii39 (2014).

42. T.-W. Kim et al., "Imaging of the lamina cribrosa in glaucoma: perspectives of pathogenesis and clinical applications," *Current Eye Res.* **38**(9), 903–909 (2013).
43. M. Yamanari, S. Makita, and Y. Yasuno, "Polarization-sensitive swept-source optical coherence tomography with continuous source polarization modulation," *Opt. Express* **16**(8), 5892–5906 (2008).
44. S. Fialová et al., "Posterior rat eye during acute intraocular pressure elevation studied using polarization sensitive optical coherence tomography," *Biomed. Opt. Express* **8**(1), 298–314 (2017).
45. V. Gruev, R. Perkins, and T. York, "CCD polarization imaging sensor with aluminum nanowire optical filters," *Opt. Express* **18**(18), 19087–19094 (2010).
46. B. Yang et al., "Polarized light spatial frequency domain imaging for non-destructive quantification of soft tissue fibrous structures," *Biomed. Opt. Express* **6**(4), 1520–1533 (2015).
47. J. Reh binder et al., "Ex vivo Mueller polarimetric imaging of the uterine cervix: a first statistical evaluation," *J. Biomed. Opt.* **21**(7), 071113 (2016).
48. F. Fereidouni et al., "Microscopy with ultraviolet surface excitation for rapid slide-free histology," *Nat. Biomed. Eng.* **1**(12), 957–966 (2017).
49. A. Pierangelo et al., "Ex-vivo characterization of human colon cancer by Mueller polarimetric imaging," *Opt. Express* **19**(2), 1582–1593 (2011).
50. K. Twietmeyer et al., "Mueller matrix retinal imager with optimized polarization conditions," *Opt. Express* **16**(26), 21339–21354 (2008).
51. R. Grytz et al., "Material properties of the posterior human sclera," *J. Mech. Behav. Biomed. Mater.* **29**, 602–617 (2014).
52. J. D. Pyne et al., "Sequential-digital image correlation for mapping human posterior sclera and optic nerve head deformation," *J. Biomech. Eng.* **136**(2), 021002 (2014).
53. B. Yang et al., "Structured polarized light microscopy (SPLM) for mapping collagen fiber orientation of ocular tissues," *Proc. SPIE* **10546**, 105460I (2018).

Biographies for the authors are not available.